

Magnetoelastic coupling and effects of uniaxial strain in α - RuCl_3 from first principles

David A. S. Kaib,^{1,*} Sananda Biswas,¹ Kira Riedl,¹ Stephen M. Winter,^{1,2} and Roser Valentí¹

¹*Institut für Theoretische Physik, Goethe-Universität Frankfurt, Max-von-Laue-Strasse 1, 60438 Frankfurt am Main, Germany*

²*Department of Physics and Center for Functional Materials, Wake Forest University, Winston-Salem, North Carolina 27109, USA*

(Dated: April 12, 2021)

We present first-principles results on the magnetoelastic coupling in α - RuCl_3 and uncover a striking dependence of the magnetic coupling constants on strain effects. Different magnetic interactions are found to respond very unequally to variations in the lattice, with the Kitaev interaction being the most sensitive. Exact diagonalization results on our magnetoelastic model reproduce recent measurements of the structural Grüneisen parameter and explain the origin of the negative magnetostriction of α - RuCl_3 , disentangling contributions related to different anisotropic interactions and g factors. Uniaxial strain perpendicular to the honeycomb planes is predicted to reorganize the relative coupling strengths, strongly enhancing the Kitaev interaction while simultaneously weakening the other anisotropic exchanges under compression. Uniaxial strain may therefore pose a fruitful route to experimentally tune α - RuCl_3 nearer to the Kitaev limit.

The exactly solvable Kitaev honeycomb model [1] features a quantum spin liquid (QSL) with non-Abelian anyons under magnetic fields. Following the proposal to realize the highly frustrated Kitaev interaction in real materials through an intricate exchange mechanism [2], so-called “Kitaev-candidate materials” emerged [3–5]. These are spin-orbit Mott insulators, whose low-energy magnetic degrees of freedom can be described through $j_{\text{eff}} = 1/2$ *pseudospins*. So far, most candidate materials exhibit long-range ordered magnetic ground states [6–11] instead of the Kitaev QSL due to residual extended interactions beyond the pure Kitaev model [11–16]. Nevertheless, the physics of such extended Kitaev models have led to countless interesting unconventional phenomena in these materials with arguably the most prominent example being α - RuCl_3 . With the goal of tuning away from its antiferromagnetic zigzag order and possibly to a Kitaev QSL, various routes have been considered, including chemical doping [17–19], graphene substrates [20–23], hydrostatic pressure [24–28] and magnetic fields [29–36]. In the case of hydrostatic pressure, dimerization quickly destroys the $j_{\text{eff}} = 1/2$ picture [24, 28] such that no Kitaev QSL can occur. α - RuCl_3 under magnetic fields has however attracted great attention, due to the observation of a narrow field-induced regime of quantized thermal Hall conductivity [33, 35, 36]. Subsequent theoretical studies highlighted the importance of magnetoelastic coupling for the description of the thermal Hall conductivity [37, 38] and investigated further consequences of magnetoelastic coupling [39, 40], in both cases for the idealized pure Kitaev model. The behavior of the longitudinal thermal conductivity under magnetic field already implies a strongly magnetoelastically-coupled phonon heat transport [41, 42]. Therefore realistic microscopic modeling of magnetoelastic coupling, taking the actual lattice and the extended (non-Kitaev) interactions into account, is crucial in tackling this key issue of α - RuCl_3 . In contrast to conventional spin-lattice

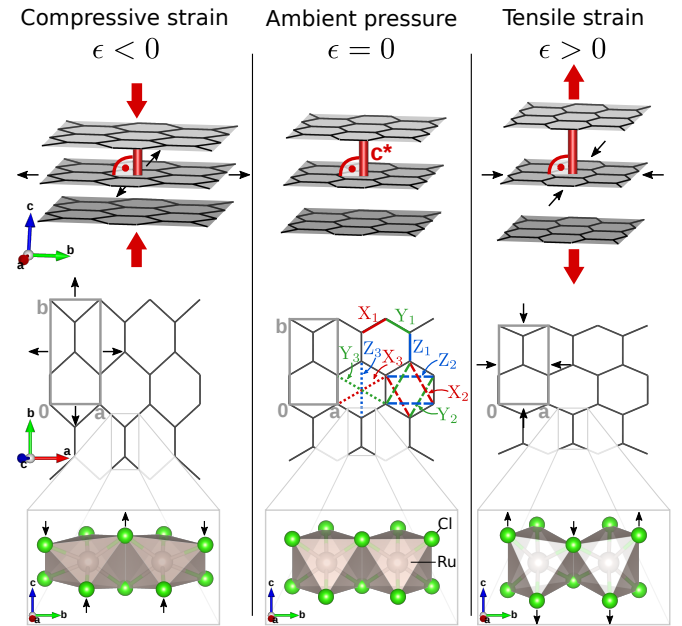


FIG. 1. Structural effects as a consequence of compressive [left column] and tensile [right column] uniaxial strain onto c^* . The middle column shows the unstrained structure. Enforced strains are indicated by red arrows and predicted responses of the system by black arrows. Shown from top to bottom are: Honeycomb layers, view onto one layer, and Ru-Ru bond with chlorine environment.

coupling, both the spin-orbital nature of the pseudospins [43, 44] and the geometry-sensitive exchange mechanisms of Kitaev materials [2, 3, 45] indicate *pseudospin*-lattice coupling to be more delicate.

In this Letter we explore how the extended interactions in α - RuCl_3 are coupled to *uniaxial* strain. Here we focus on strain perpendicular to the honeycomb planes (parallel to c^* , see Fig. 1), as it should be the direction easiest to tune experimentally and as its magnetostriction has been measured recently [46]. By combin-

ing first-principles simulations and exact diagonalization we unveil a subtle dependence of the magnetic coupling constants on strain effects and provide a microscopic understanding of magnetoelastic properties in α -RuCl₃.

Magnetoelastic model.— We first derive the magnetoelastic Hamiltonian of α -RuCl₃ under a magnetic field \mathbf{B} with uniaxial strain $\epsilon \equiv \Delta c^*/c_0^*$ as a degree of freedom,

$$\mathcal{H} = \sum_{ij} \mathbf{S}_i \cdot \mathbb{J}_{ij}(\epsilon) \cdot \mathbf{S}_j - \mu_B \sum_i \mathbf{B} \cdot \mathbb{G}(\epsilon) \cdot \mathbf{S}_i. \quad (1)$$

c^* is the distance between the honeycomb layers [Fig. 1] and \mathbf{S}_i are $j_{\text{eff}} = 1/2$ operators. The strain-dependent tensors $\mathbb{J}_{ij}(\epsilon)$ and $\mathbb{G}(\epsilon)$ contain all exchange and g -tensor couplings. Our primary objective is then to extract the strengths of the linear magnetoelastic couplings $\tilde{\mathcal{J}} \equiv \left. \frac{\partial \mathcal{J}}{\partial \epsilon} \right|_{\epsilon=0}$ for all components $\mathcal{J} \in \mathbb{J}_{ij}$ and $\mathcal{J} \in \mathbb{G}$. This way we (i) explore uniaxial strain as a potential tuning parameter in future experiments and (ii) enable theoretical modeling of observables that directly couple magnetic and structural degrees of freedom. We then apply our obtained magnetoelastic model to the field-dependent structural Grüneisen parameter and magnetostriction, finding good agreement with recent measurements [46].

For Kitaev materials the interaction tensor \mathbb{J}_{ij} is highly anisotropic and bond-directional-dependent. Bond types called X_n, Y_n and Z_n are defined on n th-nearest neighbors as shown in the center of Fig. 1. The exchange is then

$$\mathbb{J}_{ij} = \begin{pmatrix} \alpha & \beta & \gamma \\ \alpha & J_n & \Gamma_n + D_n^\gamma & \Gamma_n' - D_n^\beta \\ \beta & \Gamma_n - D_n^\gamma & J_n & \Gamma_n' + D_n^\alpha \\ \gamma & \Gamma_n' + D_n^\beta & \Gamma_n' - D_n^\alpha & J_n + K_n \end{pmatrix}, \quad (2)$$

where $(\alpha, \beta, \gamma) = (x, y, z)$ for Z_n -bonds, (y, z, x) for X_n , and (z, x, y) for Y_n -bonds. When K_1 is the only finite coupling, the model reduces to the exactly solvable Kitaev model [1]. The Dzyaloshinskii-Moriya interaction ($D_n^\alpha, D_n^\beta, D_n^\gamma$) vanishes for $n = 1, 3$ due to inversion symmetry. For simplicity we employ C_3 -symmetrized models throughout this manuscript, such that coupling strengths on X_n -, Y_n - and Z_n -bonds are equal for a given n . Deviations from this C_3 -symmetry within the $C2/m$ space group are discussed in Supplemental Material (SM) [47].

First-principles methods.— To include effects beyond a homogeneous elongation of the lattice with c^* -strain, we employ constrained geometric optimizations. To obtain a zero-strain starting structure, the ambient-pressure experimental $C2/m$ structure [80] was fully relaxed, including all lattice parameters and internal atomic positions. Subsequently, the lattice parameters a, b , monoclinic angle β , and atomic positions were relaxed while constraining c to different values. For each obtained structure, the strain is then $\epsilon = \Delta c^*/c_0^*$, with $c^* = c \sin \beta$ and c_0^* denoting the unstrained parameter. The constrained relaxations were performed within GGA+ U [47, 59] in

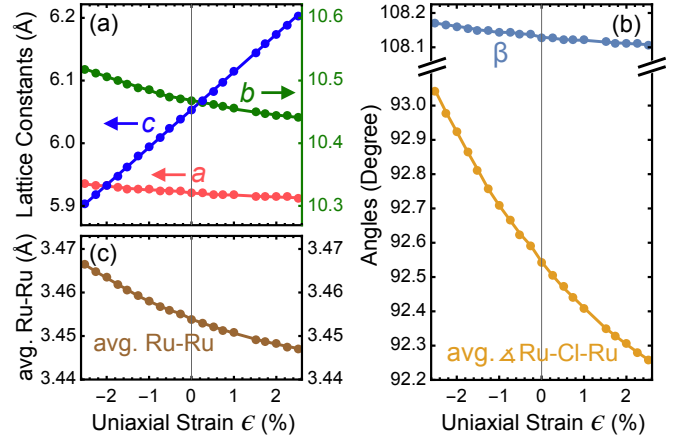


FIG. 2. Relaxed lattice parameters as a function of uniaxial strain on c^* . (a) Lattice constants. b is to be read with the right axis. (b) Monoclinic angle β and angle of the Ru-Cl-Ru bonds (average over X_1, Y_1, Z_1 bonds). (c) Average Ru-Ru bond length.

zigzag antiferromagnetic configurations using Quantum Espresso [58].

To determine the strain-dependent g -tensor components, we computed \mathbb{G} for each relaxed geometry on $[\text{RuCl}_6]^{3-}$ molecules with the quantum chemistry ORCA 3.03 package [78, 81] with the functional TPSSh, basis set def2-TZVP, and complete active space for the d orbitals CAS(5,5) — an approach that has proved reliable for isolated d^5 molecules [82].

For the exchange interactions $\mathbb{J}_{ij}(\epsilon)$, we first computed non-relativistic hopping parameters for each relaxed structure in non-spin-polarized configurations within GGA using the Full Potential Local Orbital (FPLO) code [83]. Magnetic interactions were then estimated via exact diagonalization of the two-site five-orbital Hubbard Hamiltonian and projection of the low-energy states onto the $j_{\text{eff}} = 1/2$ subspace [76, 84]. Here, we considered both t_{2g} and e_g orbitals explicitly, extending on previous approaches of some of the authors [76]. Further details on first-principles calculations are given in SM [47].

First-principles results.— The predicted effects of compressive (negative) and tensile (positive) uniaxial strain on the structure are summarized in Fig. 1 (showing illustrative extreme strains). Quantitative results are shown in Fig. 2. Upon compression along c^* , the honeycomb ab plane expands, increasing the Ru-Ru distance. Importantly, the octahedral chlorine environment, whose precise geometry mainly governs the Jackeli-Khaliulin exchange mechanism [2, 3, 73], is distorted in a strongly non-homogeneous way under uniaxial strain, see bottom row of Fig. 1.

The magnetoelastic couplings $\tilde{\mathcal{J}} \equiv \left. \frac{\partial \mathcal{J}}{\partial \epsilon} \right|_{\epsilon=0}$ for each g -value ($\mathcal{J} \in \mathbb{G}$) and magnetic coupling parameter ($\mathcal{J} \in \mathbb{J}_{ij}$) were determined by differentiating third-order polynomial fits to their strain-dependencies as illus-

	g_{ab}	g_{c^*}	J_1	K_1	Γ_1	Γ'_1	J_2	K_2	Γ_2	Γ'_2	D_2^α	D_2^β	D_2^γ	J_3	K_3	Γ_3	Γ'_3
$\mathcal{J} _{\epsilon=0}$	2.36	1.88	-5.7	-10.1	9.3	-0.7	0.	-0.2	0.1	0.	0.	0.1	0.1	0.2	0.2	0.	-0.1
$\tilde{\mathcal{J}}$	-1.6	3.85	1.3	40.5	7.5	-11.5	-0.9	1.6	-0.4	-0.1	-1.	-1.	-3.2	1.6	0.6	-0.6	-0.5

TABLE I. C_3 -symmetrized magnetic couplings at ambient pressure $\mathcal{J}|_{\epsilon=0}$ and the associated magnetoelastic couplings $\tilde{\mathcal{J}} \equiv (\partial\mathcal{J}/\partial\epsilon)|_{\epsilon=0}$. Except for unitless g -tensor components, units are in meV. Strongest couplings are highlighted.

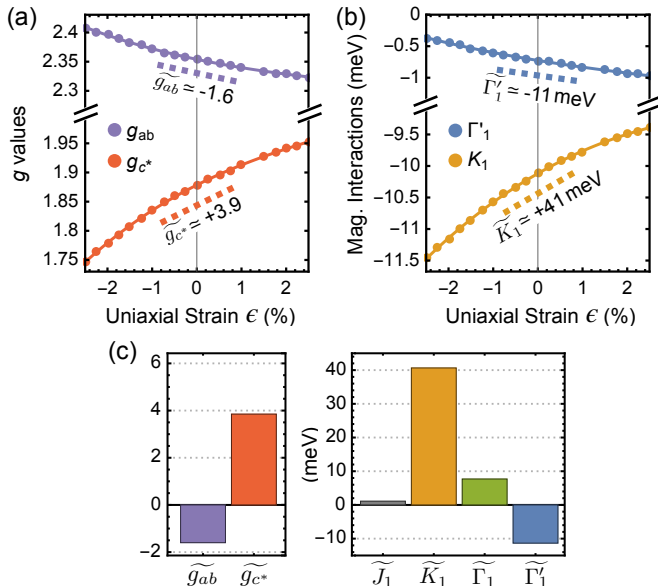


FIG. 3. (a) Calculated strain-dependence of g values and (b) K_1 , Γ'_1 (colored bullets). Solid curves show third-order polynomial fits. Dashed lines indicate $\tilde{\mathcal{J}} \equiv (\partial\mathcal{J}/\partial\epsilon)|_{\epsilon=0}$. (c) Comparison of magnetoelastic couplings $\tilde{\mathcal{J}}$ for g values and nearest-neighbor interactions.

trated exemplary in Fig. 3(a,b) for the couplings with the strongest strain-dependence. Corresponding magnetoelastic couplings of the g values and nearest-neighbor interactions are compared in Fig. 3(c). The complete set of obtained ambient-pressure model parameters $\mathcal{J}|_{\epsilon=0}$ and $\tilde{\mathcal{J}}$ is listed in Table I, with large couplings highlighted.

The gyromagnetic tensor \mathbb{G} of each magnetic site is determined mainly by its local chlorine environment. Due to the non-trivial distortion under uniaxial strain ϵ [Fig. 1], the strain-dependence of the g -anisotropy cannot be explained with regular expressions [85] that are valid for trigonally compressed octahedral environments. From *ab-initio*, the non-negligible components of \mathbb{G} for the zero-strain structure are found to be: $g_{ab} = 2.36$ (in-plane) and $g_{c^*} = 1.88$ (out-of-plane), which fall in the range of existing estimates [49, 85–87]. For their magnetoelastic couplings, we extract $\tilde{g}_{ab} = -1.6$ and $\tilde{g}_{c^*} = 3.85$. Compressive strain $\epsilon < 0$ will therefore increase g_{ab} and decrease g_{c^*} , enhancing the g anisotropy further, see Fig. 3(a).

The magnetic interactions \mathbb{J}_{ij} are mainly governed by the corresponding Ru-Ru distances and the Ru-Cl-Ru

geometry [Fig. 2(b,c)] through modified orbital overlap integrals. Inclusion of virtual processes involving the e_g orbitals is found to strongly renormalize some interactions [47], doubling, for example, the magnitude of the Kitaev exchange K_1 . This interaction constitutes the strongest coupling in the ambient-strain model ($K_1 = -10.1$ meV) and has the strongest strain dependence ($\tilde{K}_1 = 40.5$ meV), see Fig. 3(c). The fact that the large \tilde{K}_1 has opposite sign of K_1 implies that *compressive* strain ($\epsilon < 0$) firmly *strengthens* the Kitaev interaction. Regarding the results on the set of extended interactions as a whole, we emphasize that uniaxial strain affects different interactions unequally, strengthening some while weakening others — in contrast to effects predicted for volumetric strain or hydrostatic pressure [27]. Inspecting again the effect of compressive c^* -strain, the shared sign of $\tilde{\Gamma}_1$ with Γ_1 implies that $|\Gamma_1|$ will be *weakened*, which analogously holds for $|\Gamma'_1|$. The structure of the largest magnetoelastic couplings [bold in second row of Table I] therefore implies that compressive c^* -strain predominantly shifts interaction strength away from these anisotropic couplings and towards the Kitaev exchange K_1 .

Contrary to what one may expect, c^* -strain predominantly couples to these in-plane interactions, whereas *inter-plane* magnetoelastic couplings are found to be much weaker [47]. Experiments probing c^* -variations are therefore highly sensitive to the in-plane magnetism.

Discussion.— For the application of our derived models we first focus on primarily magnetic observables. These are determined mainly by the zero-strain interactions $\mathcal{J}|_{\epsilon=0}$ [first row in Table I] and can be computed using ED in the projected $j_{\text{eff}} = 1/2$ basis on a hexagon-shaped 24-site cluster. Throughout, we find very good agreement with experimental observations. In particular, the zigzag-ordered ground state, correct critical field strengths [29, 30] and the evolution of the magnetic torque [50–52] and magnetotropic coefficient [51, 53] are captured. Peculiarly, a ferromagnetic phase is highly proximate to the ground state, and zigzag order is only upheld by the weak $\Gamma'_1 = -0.7$ meV. The large $\tilde{\Gamma}'_1 = -11.5$ meV therefore implies that compressive c^* -strain should strongly destabilize zigzag order. Detailed results for magnetic properties are shown in SM [47].

Our main focus lies on *magnetoelastic* properties, which are driven by $\tilde{\mathcal{J}}$. Motivated by recent measurements by Gass *et al.* [46], we focus on linear magnetostriction $\lambda_{c^*} \equiv c^{*-1}(\partial c^*/\partial B)$ and the structural Grüneisen

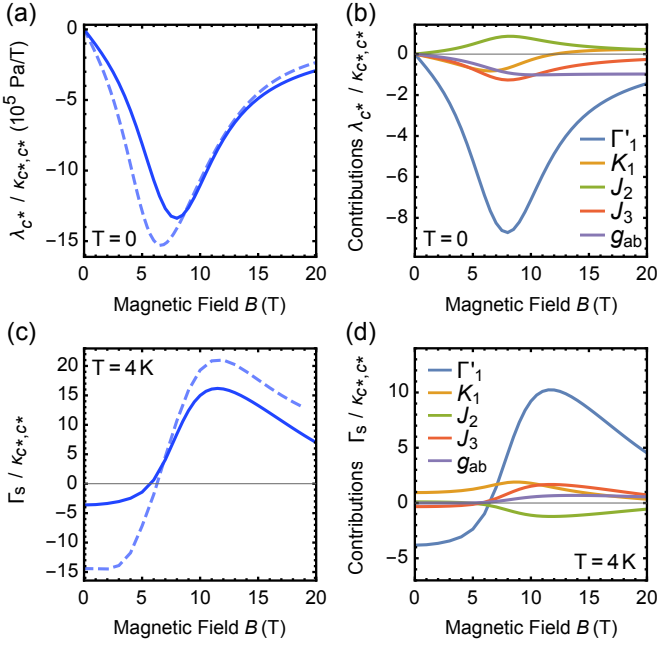


FIG. 4. (a) Calculated field-dependent magnetostriction at $T = 0$ K and (c) structural Grüneisen parameter at 4 K. $\mathbf{B} \parallel b$. (b,d) Dissection of the largest contributions to the respective quantities via Eqs. (3) and (4). Solid lines: Obtained using all $\tilde{\mathcal{J}}$ and $\mathcal{J}|_{\epsilon=0}$ from Table I. Dashed lines: Using all $\tilde{\mathcal{J}}$ from Table I and $\mathcal{J}|_{\epsilon=0}$ from the model of Ref. 55.

parameter $\Gamma_s \equiv -\frac{(\partial S_m / \partial p_{c^*})}{T(\partial S_m / \partial T)}$. Here p_{c^*} is uniaxial pressure along c^* and S_m the magnetic entropy, which the authors of Ref. 46 obtained via subtraction of phononic contributions. Under the assumption that the diagonal components of the elasticity tensor are dominant, the observables can be approximated [47]

$$\lambda_{c^*} \approx \frac{\kappa_{c^*c^*}}{V} \sum_{\mathcal{J} \in \{J_1, K_1, \dots, g_{ab}, g_{c^*}\}} \tilde{\mathcal{J}} \left(\frac{\partial M}{\partial \mathcal{J}} \right)_{\epsilon=0}, \quad (3)$$

$$\Gamma_s \approx \frac{\kappa_{c^*c^*}}{T} \sum_{\mathcal{J} \in \{J_1, K_1, \dots, g_{ab}, g_{c^*}\}} \tilde{\mathcal{J}} \left(\frac{\partial S_m}{\partial \mathcal{J}} \right)_{\epsilon=0} \left(\frac{\partial S_m}{\partial T} \right)_{\epsilon=0}^{-1}, \quad (4)$$

where the sums go over all strain-dependent interactions and g values: $\mathcal{J} \in \{J_1, K_1, \dots, g_{ab}, g_{c^*}\}$. The magnetoelastic couplings $\tilde{\mathcal{J}}$ are taken from Table I and the derivatives are evaluated at $\epsilon = 0$ (*i.e.*, at parameters $\mathcal{J}|_{\epsilon=0}$) within ED. We compute quantities up to the unknown $\kappa_{c^*c^*} \equiv -(\partial \epsilon / \partial p_{c^*})$ of α -RuCl₃, defined as the linear compressibility along c^* against *uniaxial* pressure p_{c^*} .

In Fig. 4 we present results for λ_{c^*} and Γ_s obtained from the Table I parameters as solid curves (dashed curves are discussed below). Fig. 4(a) shows the $T \rightarrow 0$ magnetostriction λ_{c^*} as a function of in-plane field $\mathbf{B} \parallel b$. The magnetostriction exhibits its maximum magnitude at the critical field of the model ($B_c \approx 7.5$ T). Note that finite-size effects in ED typically broaden features near the critical field, hence λ_{c^*} is expected to peak sharper

at B_c in the thermodynamic limit [47]. For increasing field strengths $B > B_c$, the magnitude of λ_{c^*} shrinks monotonically. The *negative* magnetostriction throughout implies a field-induced compression of α -RuCl₃. We therefore find very good agreement with experiment [46], although it is not clear whether a subtle reported kink above B_c [46] is also present in our results.

The form of Eq. (3) allows to dissect individual contributions to the magnetostriction, $\tilde{\mathcal{J}} \cdot (\partial M / \partial \mathcal{J})$, stemming from the interplay of different interactions \mathcal{J} with the lattice. One may expect that the magnetostriction would be influenced strongly by the summand with $\mathcal{J} = K_1$ due to the large \tilde{K}_1 (cf. Fig. 3(c)). However, we find the associated magnetization susceptibility ($\partial M / \partial K_1$) to be negligible in magnitude compared to other magnetization susceptibilities. Instead, the magnetostriction is found to be governed by the summand with $\mathcal{J} = \Gamma'_1$, as shown in Fig. 4(b). Here $(\partial M / \partial \Gamma'_1) > 0$, which can already be anticipated on the classical level [47], and $\tilde{\Gamma}'_1 < 0$. The negative magnetostriction may therefore be understood as follows: Under increased B , α -RuCl₃ can lower its Zeeman energy further (*i.e.*, increase its magnetization) by *increasing* $\tilde{\Gamma}'_1$ ($\partial M / \partial \tilde{\Gamma}'_1 > 0$), which is achieved by *c^* -compression* ($\tilde{\Gamma}'_1 < 0$).

We now turn to the structural Grüneisen parameter Γ_s , computed via Eq. (4) and ED. Here, we achieve finite temperatures by restricting the canonical sums to the lowest 16 eigenstates, which works well for lowest temperatures [47]. Results are shown in Fig. 4(c,d). We again find a good qualitative agreement with experiment [46], with a sign change from negative to positive near $B = B_c$. Likely because of finite-size effects, the slope at the sign change is not vertical, and Γ_s only reaches its maximum for fields slightly above B_c . In contrast to experiment, we obtain $|\Gamma_s(B \lesssim B_c)| < |\Gamma_s(B \gtrsim B_c)|$. Dissecting the contributions from different magnetoelastic couplings in Fig. 4(d), we again find that the contribution related to $\tilde{\Gamma}'_1$ dominates the magnetoelastic response. Analyzing our results for temperatures below that of the experiment (4 K), we predict most of the qualitative response to be unchanged. However, we note that our model also predicts an anomalous drop in both the structural (Γ_s) and magnetic (Γ_B) Grüneisen parameters at high fields $B \approx 22$ T [47, 57], which becomes increasingly sharp at lower temperatures. Experimentally, such an anomaly was clearly observed in Γ_B around $B \approx 10$ T at $T < 2$ K [57], and is also suggested by recent data on Γ_s at $T = 3.5$ K in the same field range [46]. These anomalies are understood to occur due to interchange of lowest excited states [57], which occurs at a field strength that is highly sensitive to the specific couplings. This may be considered for future refinements of the model.

In the results discussed so far, we employed the complete set of magnetic interactions $\mathcal{J}|_{\epsilon=0}$ and magnetoelastic couplings $\tilde{\mathcal{J}}$ from Table I. However, our re-

sults on the magnetoelastic coupling may also provide guidelines for theoretical modeling in reduced parameter spaces. Therefore we also considered a *minimal* magnetic model $\{\mathcal{J}|_{\epsilon=0}\}$ with only four nonzero interactions, $(J_1, K_1, \Gamma_1, J_3) = (-0.5, -5.0, 2.5, 0.5)$ meV and $g_{ab} = 2.3$, which has reproduced key experimental observations on magnetic properties [29, 49, 54, 55, 57, 87, 88]. We repeated our calculations, evaluating the derivatives in Eqs. (3) and (4) at these minimal-model values $\mathcal{J}|_{\epsilon=0}$ (keeping the magnetoelastic couplings $\tilde{\mathcal{J}}$ from Table I). Results are shown as dashed lines in Fig. 4(a,c). Overall, the results are comparable to before. Note — importantly — that a summand in Eqs. (3) and (4) related to $\tilde{\mathcal{J}}$ is *not* required to vanish if the respective $\mathcal{J}|_{\epsilon=0}$ is zero. On the contrary, we find also in the case of this minimal model that contributions from the magnetoelastic coupling $\tilde{\Gamma}'_1$ essentially dominate the response, regardless of $\Gamma'_1|_{\epsilon=0} = 0$. This highlights that the dominant magnetoelastic interactions in α -RuCl₃ can be of completely different form than the dominant ambient-pressure magnetic interactions.

Conclusions.— We derived a magnetoelastic Hamiltonian for α -RuCl₃ completely from *ab-initio*. We have shown that it reproduces key magnetic phenomena of α -RuCl₃ and can explain recent field-dependent structural Grüneisen and magnetostriction measurements [46]. For magnetoelastic properties, a $\tilde{\Gamma}'_1$ -type magnetoelastic coupling (“ $\tilde{\Gamma}'_1$ ”) is found to dominate, albeit the associated interaction Γ'_1 being subdominant in the purely magnetic part of the Hamiltonian. Such non-Kitaev magnetoelastic effects should be reconsidered when comparing pure-Kitaev pseudospin-phonon modeling with experiments. Compressive uniaxial strain perpendicular to the honeycomb planes is predicted to strongly destabilize zigzag order while shifting interaction strength from other anisotropic couplings towards the Kitaev exchange. The strong reorganization of the magnetic interactions by uniaxial strain is a result of the geometry-sensitive exchange mechanisms in Kitaev materials and therefore likely extends also to other two- and three-dimensional Kitaev materials. The methodology we explored in this study is extendable to other materials and arbitrary strain fields. It enables to tackle quantitatively the pseudospin-phonon couplings, that may play a crucial role in understanding the thermal Hall conductivity.

Note added: After completion of this work, several experimental studies were posted that further highlight the importance of magnetoelastic coupling in α -RuCl₃ [42, 89, 90].

Acknowledgments.— We thank Anja Wolter and Bernd Büchner for fruitful discussions and we acknowledge the Deutsche Forschungsgemeinschaft (DFG, German Research Foundation) for funding through Project No. 411289067 (VA117/15-1) and TRR 288 - 422213477 (project A05).

* kaib@itp.uni-frankfurt.de

- [1] A. Kitaev, *Ann. Phys.* **321**, 2 (2006).
- [2] G. Jackeli and G. Khaliullin, *Phys. Rev. Lett.* **102**, 017205 (2009).
- [3] S. M. Winter, A. A. Tsirlin, M. Daghofer, J. van den Brink, Y. Singh, P. Gegenwart, and R. Valenti, *J. Phys.: Condens. Matter* **29**, 493002 (2017).
- [4] M. Hermanns, I. Kimchi, and J. Knolle, *Annu. Rev. Condens. Matter Phys.* **9**, 17 (2018).
- [5] H. Takagi, T. Takayama, G. Jackeli, G. Khaliullin, and S. E. Nagler, *Nat. Rev. Phys.* **1**, 264 (2019).
- [6] X. Liu, T. Berlijn, W.-G. Yin, W. Ku, A. Tsvelik, Y.-J. Kim, H. Gretarsson, Y. Singh, P. Gegenwart, and J. P. Hill, *Phys. Rev. B* **83**, 220403(R) (2011).
- [7] F. Ye, S. Chi, H. Cao, B. C. Chakoumakos, J. A. Fernandez-Baca, R. Custelcean, T. F. Qi, O. B. Korneta, and G. Cao, *Phys. Rev. B* **85**, 180403(R) (2012).
- [8] A. Biffin, R. D. Johnson, S. Choi, F. Freund, S. Manni, A. Bombardi, P. Manuel, P. Gegenwart, and R. Coldea, *Phys. Rev. B* **90**, 205116 (2014).
- [9] J. A. Sears, M. Songvilay, K. W. Plumb, J. P. Clancy, Y. Qiu, Y. Zhao, D. Parshall, and Y.-J. Kim, *Phys. Rev. B* **91**, 144420 (2015).
- [10] R. D. Johnson, S. C. Williams, A. A. Haghighirad, J. Singleton, V. Zapf, P. Manuel, I. I. Mazin, Y. Li, H. O. Jeschke, R. Valentí, *et al.*, *Phys. Rev. B* **92**, 235119 (2015).
- [11] S. C. Williams, R. D. Johnson, F. Freund, S. Choi, A. Jesche, I. Kimchi, S. Manni, A. Bombardi, P. Manuel, P. Gegenwart, and R. Coldea, *Phys. Rev. B* **93**, 195158 (2016).
- [12] J. Chaloupka, G. Jackeli, and G. Khaliullin, *Phys. Rev. Lett.* **105**, 027204 (2010).
- [13] J. Chaloupka, G. Jackeli, and G. Khaliullin, *Phys. Rev. Lett.* **110**, 097204 (2013).
- [14] J. G. Rau, E. K.-H. Lee, and H.-Y. Kee, *Phys. Rev. Lett.* **112**, 077204 (2014).
- [15] A. Biffin, R. D. Johnson, I. Kimchi, R. Morris, A. Bombardi, J. G. Analytis, A. Vishwanath, and R. Coldea, *Phys. Rev. Lett.* **113**, 197201 (2014).
- [16] E. K.-H. Lee and Y. B. Kim, *Phys. Rev. B* **91**, 064407 (2015).
- [17] A. Koitzsch, C. Habenicht, E. Müller, M. Knupfer, B. Büchner, S. Kretschmer, M. Richter, J. van den Brink, F. Börrnert, D. Nowak, *et al.*, *Phys. Rev. Mater.* **1**, 052001 (2017).
- [18] G. Bastien, M. Roslova, M. H. Haghighi, K. Mehlawat, J. Hunger, A. Isaeva, T. Doert, M. Vojta, B. Büchner, and A. U. B. Wolter, *Phys. Rev. B* **99**, 214410 (2019).
- [19] S.-H. Baek, H. W. Yeo, S.-H. Do, K.-Y. Choi, L. Janssen, M. Vojta, and B. Büchner, *Phys. Rev. B* **102**, 094407 (2020).
- [20] S. Mashhadi, Y. Kim, J. Kim, D. Weber, T. Taniguchi, K. Watanabe, N. Park, B. Lotsch, J. H. Smet, M. Burghard, *et al.*, *Nano Letters* **19**, 4659 (2019).
- [21] B. Zhou, J. Balgley, P. Lampen-Kelley, J.-Q. Yan, D. G. Mandrus, and E. A. Henriksen, *Phys. Rev. B* **100**, 165426 (2019).
- [22] S. Biswas, Y. Li, S. M. Winter, J. Knolle, and R. Valentí, *Phys. Rev. Lett.* **123**, 237201 (2019).
- [23] E. Gerber, Y. Yao, T. A. Arias, and E.-A. Kim, *Phys.*

- Rev. Lett. **124**, 106804 (2020).
- [24] T. Biesner, S. Biswas, W. Li, Y. Saito, A. Pustogow, M. Altmeyer, A. U. B. Wolter, B. Büchner, M. Roslova, T. Doert, *et al.*, Phys. Rev. B **97**, 220401(R) (2018).
- [25] G. Bastien, G. Garbarino, R. Yadav, F. J. Martinez-Casado, R. Beltrán Rodríguez, Q. Stahl, M. Kusch, S. P. Limandri, R. Ray, P. Lampen-Kelley, *et al.*, Phys. Rev. B **97**, 241108(R) (2018).
- [26] Z. Wang, J. Guo, F. F. Tafti, A. Hegg, S. Sen, V. A. Sidorov, L. Wang, S. Cai, W. Yi, Y. Zhou, *et al.*, Phys. Rev. B **97**, 245149 (2018).
- [27] R. Yadav, S. Rachel, L. Hozoi, J. van den Brink, and G. Jackeli, Phys. Rev. B **98**, 121107(R) (2018).
- [28] G. Li, X. Chen, Y. Gan, F. Li, M. Yan, F. Ye, S. Pei, Y. Zhang, L. Wang, H. Su, *et al.*, Phys. Rev. Mater. **3**, 023601 (2019).
- [29] A. U. B. Wolter, L. T. Corredor, L. Janssen, K. Nenkov, S. Schönecker, S.-H. Do, K.-Y. Choi, R. Albrecht, J. Hunger, T. Doert, *et al.*, Phys. Rev. B **96**, 041405(R) (2017).
- [30] S.-H. Baek, S.-H. Do, K.-Y. Choi, Y. S. Kwon, A. U. B. Wolter, S. Nishimoto, J. van den Brink, and B. Büchner, Phys. Rev. Lett. **119**, 037201 (2017).
- [31] Z. Wang, S. Reschke, T. Hübner, S.-H. Do, K.-Y. Choi, M. Gensch, U. Nagel, T. Rööm, and A. Loidl, Phys. Rev. Lett. **119**, 227202 (2017).
- [32] A. Banerjee, P. Lampen-Kelley, J. Knolle, C. Balz, A. A. Aczel, B. Winn, Y. Liu, D. Pajerowski, J. Yan, C. A. Bridges, *et al.*, npj Quantum Mater. **3**, 8 (2018).
- [33] Y. Kasahara, T. Ohnishi, Y. Mizukami, O. Tanaka, S. Ma, K. Sugii, N. Kurita, H. Tanaka, J. Nasu, Y. Motome, *et al.*, Nature **559**, 227 (2018).
- [34] C. Balz, P. Lampen-Kelley, A. Banerjee, J. Yan, Z. Lu, X. Hu, S. M. Yadav, Y. Takano, Y. Liu, D. A. Tennant, *et al.*, Phys. Rev. B **100**, 060405(R) (2019).
- [35] T. Yokoi, S. Ma, Y. Kasahara, S. Kasahara, T. Shibauchi, N. Kurita, H. Tanaka, J. Nasu, Y. Motome, C. Hickey, *et al.*, arXiv:2001.01899.
- [36] M. Yamashita, J. Gouchi, Y. Uwatoko, N. Kurita, and H. Tanaka, Phys. Rev. B **102**, 220404 (2020).
- [37] Y. Vinkler-Aviv and A. Rosch, Phys. Rev. X **8**, 031032 (2018).
- [38] M. Ye, G. B. Halász, L. Savary, and L. Balents, Phys. Rev. Lett. **121**, 147201 (2018).
- [39] A. Metavitsiadis and W. Brenig, Phys. Rev. B **101**, 035103 (2020).
- [40] M. Ye, R. M. Fernandes, and N. B. Perkins, Phys. Rev. Res. **2**, 033180 (2020).
- [41] R. Hentrich, A. U. B. Wolter, X. Zotos, W. Brenig, D. Nowak, A. Isaeva, T. Doert, A. Banerjee, P. Lampen-Kelley, D. G. Mandrus, *et al.*, Phys. Rev. Lett. **120**, 117204 (2018).
- [42] R. Hentrich, X. Hong, M. Gillig, F. Caglieris, M. Čulo, M. Shahrokhvand, U. Zeitler, M. Roslova, A. Isaeva, Doert, *et al.*, Phys. Rev. B **102**, 235155 (2020).
- [43] H. Liu and G. Khaliullin, Phys. Rev. Lett. **122**, 057203 (2019).
- [44] J. Porras, J. Bertinshaw, H. Liu, G. Khaliullin, N. H. Sung, J.-W. Kim, S. Francoual, P. Steffens, G. Deng, M. M. Sala, *et al.*, Phys. Rev. B **99**, 085125 (2019).
- [45] J. G. Rau, E. K.-H. Lee, and H.-Y. Kee, Annu. Rev. Condens. Matter Phys. **7**, 195 (2016).
- [46] S. Gass, P. M. Cónsoli, V. Kocsis, L. T. Corredor, P. Lampen-Kelley, D. G. Mandrus, S. E. Nagler, L. Janssen, M. Vojta, B. Büchner, *et al.*, Phys. Rev. B **101**, 245158 (2020).
- [47] See appended Supplementary Material for details on *ab-initio* and ED methods, complete obtained *ab-initio* model parameters, ED results on primarily magnetic properties and derivation of Eqs. (3) and (4). Also contains Refs. [48-79].
- [48] H. Suzuki, H. Liu, J. Bertinshaw, K. Ueda, H. Kim, S. Laha, D. Weber, Z. Yang, L. Wang, H. Takahashi, *et al.*, arXiv:2008.02037.
- [49] S. M. Winter, K. Riedl, D. Kaib, R. Coldea, and R. Valentí, Phys. Rev. Lett. **120**, 077203 (2018).
- [50] I. A. Leahy, C. A. Pocs, P. E. Siegfried, D. Graf, S.-H. Do, K.-Y. Choi, B. Normand, and M. Lee, Phys. Rev. Lett. **118**, 187203 (2017).
- [51] K. A. Modic, M. D. Bachmann, B. J. Ramshaw, F. Arnold, K. R. Shirer, A. Estry, J. B. Betts, N. J. Ghimire, E. D. Bauer, M. Schmidt, *et al.*, Nat. Commun. **9**, 3975 (2018).
- [52] K. A. Modic, B. J. Ramshaw, A. Shekhter, and C. M. Varma, Phys. Rev. B **98**, 205110 (2018).
- [53] K. A. Modic, R. D. McDonald, J. P. C. Ruff, M. D. Bachmann, Y. Lai, J. C. Palmstrom, D. Graf, M. K. Chan, F. F. Balakirev, J. B. Betts, G. S. Boebinger, M. Schmidt, M. J. Lawler, D. A. Sokolov, P. J. W. Moll, B. J. Ramshaw, and A. Shekhter, Nat. Phys. **17**, 240 (2020).
- [54] K. Riedl, Y. Li, S. M. Winter, and R. Valentí, Phys. Rev. Lett. **122**, 197202 (2019).
- [55] S. M. Winter, K. Riedl, P. A. Maksimov, A. L. Chernyshev, A. Honecker, and R. Valentí, Nat. Commun. **8**, 1152 (2017).
- [56] P. A. Maksimov and A. L. Chernyshev, Phys. Rev. Res. **2**, 033011 (2020).
- [57] S. Bachus, D. A. S. Kaib, Y. Tokiwa, A. Jesche, V. Tsurkan, A. Loidl, S. M. Winter, A. A. Tsirlin, R. Valentí, and P. Gegenwart, Phys. Rev. Lett. **125**, 097203 (2020).
- [58] P. Giannozzi, S. Baroni, N. Bonini, M. Calandra, R. Car, C. Cavazzoni, D. Ceresoli, G. L. Chiarotti, M. Cococcioni, I. Dabo, *et al.*, J. Condens. Matter Phys. **21**, 395502 (2009).
- [59] J. P. Perdew, K. Burke, and M. Ernzerhof, Phys. Rev. Lett. **77**, 3865 (1996).
- [60] S. Grimme, J. Phys. Chem. Solids **27**, 1787 (2006).
- [61] H. J. Monkhorst and J. D. Pack, Phys. Rev. B **13**, 5188 (1976).
- [62] G. Kresse and J. Hafner, Phys. Rev. B **47**, 558 (1993).
- [63] P. E. Blöchl, Phys. Rev. B **50**, 17953 (1994).
- [64] H.-S. Kim and H.-Y. Kee, Phys. Rev. B **93**, 155143 (2016).
- [65] V. Hermann, M. Altmeyer, J. Ebad-Allah, F. Freund, A. Jesche, A. A. Tsirlin, M. Hanfland, P. Gegenwart, I. I. Mazin, D. I. Khomskii, *et al.*, Phys. Rev. B **97**, 020104(R) (2018).
- [66] V. Hermann, S. Biswas, J. Ebad-Allah, F. Freund, A. Jesche, A. A. Tsirlin, M. Hanfland, D. Khomskii, P. Gegenwart, R. Valentí, *et al.*, Phys. Rev. B **100**, 064105 (2019).
- [67] A. Banerjee, J. Yan, J. Knolle, C. A. Bridges, M. B. Stone, M. D. Lumsden, D. G. Mandrus, D. A. Tennant, R. Moessner, and S. E. Nagler, Science **356**, 1055 (2017).
- [68] S.-H. Do, S.-Y. Park, J. Yoshitake, J. Nasu, Y. Motome, Y. S. Kwon, D. T. Adroja, D. J. Voneshen, K. Kim, T.-H.

- Jang, *et al.*, *Nat. phys.* **13**, 1079 (2017).
- [69] P. Lampen-Kelley, L. Janssen, E. C. Andrade, S. Rachel, J.-Q. Yan, C. Balz, D. G. Mandrus, S. E. Nagler, and M. Vojta, arXiv:1807.06192.
- [70] J. C. Slater, *Quantum theory of atomic structure* (McGraw-Hill, New York, 1960).
- [71] C. Eichstaedt, Y. Zhang, P. Laurell, S. Okamoto, A. G. Eguiluz, and T. Berlijn, *Phys. Rev. B* **100**, 075110 (2019).
- [72] M. Montalti, A. Credi, L. Prodi, and M. T. Gandolfi, *Handbook of photochemistry* (CRC press, Boca Raton, FL, 2006).
- [73] J. G. Rau and H.-Y. Kee, arXiv:1408.4811.
- [74] K. Foyevtsova, H. O. Jeschke, I. I. Mazin, D. I. Khomskii, and R. Valentí, *Phys. Rev. B* **88**, 035107 (2013).
- [75] H.-S. Kim, V. Vijay Shankar, A. Catuneanu, and H.-Y. Kee, *Phys. Rev. B* **91**, 241110(R) (2015).
- [76] S. M. Winter, Y. Li, H. O. Jeschke, and R. Valentí, *Phys. Rev. B* **93**, 214431 (2016).
- [77] Y. S. Hou, H. J. Xiang, and X. G. Gong, *Phys. Rev. B* **96**, 054410 (2017).
- [78] F. Neese, *Wiley Interdiscip. Rev. Comput. Mol. Sci.* **2**, 73 (2012).
- [79] P. Laurell and S. Okamoto, *npj Quantum Mater.* **5**, 2 (2020).
- [80] H. B. Cao, A. Banerjee, J.-Q. Yan, C. A. Bridges, M. D. Lumsden, D. G. Mandrus, D. A. Tennant, B. C. Chakoumakos, and S. E. Nagler, *Phys. Rev. B* **93**, 134423 (2016).
- [81] F. Neese, *J. Chem. Phys.* **122**, 034107 (2005).
- [82] K. S. Pedersen, J. Bendix, A. Tressaud, E. Durand, H. Weihe, Z. Salman, T. J. Morsing, D. N. Woodruff, Y. Lan, W. Wernsdorfer, *et al.*, *Nat. Commun.* **7**, 12195 (2016).
- [83] K. Koepf and H. Eschrig, *Phys. Rev. B* **59**, 1743 (1999).
- [84] K. Riedl, Y. Li, R. Valentí, and S. M. Winter, *Phys. Status Solidi B* **256**, 1800684 (2019).
- [85] J. Chaloupka and G. Khaliullin, *Phys. Rev. B* **94**, 064435 (2016).
- [86] R. Yadav, N. A. Bogdanov, V. M. Katukuri, S. Nishimoto, J. van den Brink, and L. Hozoi, *Sci. Rep.* **6**, 37925 (2016).
- [87] A. Sahasrabudhe, D. A. S. Kaib, S. Reschke, R. German, T. C. Koethe, J. Buhot, D. Kamenskyi, C. Hickey, P. Becker, V. Tsurkan, *et al.*, *Phys. Rev. B* **101**, 140410(R) (2020).
- [88] J. Cookmeyer and J. E. Moore, *Phys. Rev. B* **98**, 060412(R) (2018).
- [89] R. Schönemann, S. Imajo, F. Weickert, J. Yan, D. G. Mandrus, Y. Takano, E. L. Brosha, P. F. S. Rosa, S. E. Nagler, K. Kindo, and M. Jaime, *Phys. Rev. B* **102**, 214432 (2020).
- [90] H. Li, T. T. Zhang, A. Said, G. Fabbris, D. G. Mazzone, J. Q. Yan, D. Mandrus, G. B. Halasz, S. Okamoto, S. Murakami, *et al.*, arXiv:2011.07036.

Supplemental Material:

Magnetoelastic coupling and effects of uniaxial strain in α -RuCl₃ from first principles

Magnetic properties of the *ab-initio* derived model

We study primarily magnetic properties of the $\{\mathcal{J}|_{\epsilon=0}\}$ model given in Table I of the main text. While the physics of these properties have been covered and discussed in previous modeling, they provide comparisons to a wide array of measurements. Therefore the results presented in this section serve primarily as benchmark of our fully *ab-initio* obtained model and thus of the applied first-principles methodology. To compute different observables within the model, we employ ED in the $j_{\text{eff}} = 1/2$ basis on a hexagon-shaped 24-site cluster. We employ all 17 parameters of the main-text Table I model. Note that restricting to the nearest-neighbor couplings ($J_1, K_1, \Gamma_1, \Gamma'_1$) of this model gives similar results regarding zigzag order and critical field strengths within ED. But in the following we follow through with all parameters to consistently work with fully *ab-initio* results.

At $\mathbf{B} = 0, T = 0$, the model correctly reproduces anti-ferromagnetic zigzag order within ED, revealed by dominant static spin-spin correlations $\langle \mathbf{S}(-\mathbf{q}) \cdot \mathbf{S}(\mathbf{q}) \rangle$ at the zigzag ordering wave vectors $\mathbf{q} \in \{M, M', Y\}$. However, significant ferromagnetic correlations $\langle \mathbf{S}(0) \cdot \mathbf{S}(0) \rangle \approx 0.7 \langle \mathbf{S}(-M) \cdot \mathbf{S}(M) \rangle$ are also persistent, as a result of the strong ferromagnetic $|J_1| \approx 0.5|K_1|$ in the model (Table I of the main text). This is consistent with the conclusions of a recent study using resonant inelastic X-ray scattering [48]. In the present model, ferromagnetism is so competitive, that the ferromagnetic state ($\mathbf{q} = 0$) is lower in energy than the zigzag one on the classical level. Zigzag order found in ED is therefore likely a result of significant quantum fluctuations. The small $\Gamma'_1 = -0.7$ meV [Table I in main text] stabilizes this order, and zigzag order is lost for $\Gamma'_1 \gtrsim -0.2$ meV (keeping all other interactions unchanged) within ED. Recalling the effects of compressive c^* -strain as discussed in the main text, i.e., a strong suppression of $|\Gamma'_1|$ and $|\Gamma_1|$ together with a vast increase of $|K_1|$, we estimate compressive uniaxial strains of $\epsilon \sim -3\%$ to -5% to be sufficient to suppress zigzag order (at zero magnetic field).

We now turn to properties at finite magnetic fields \mathbf{B} . Figure S1(a) shows the magnetization as a function of field strength for in-plane fields $\mathbf{B} \parallel b$ and out-of-plane fields $\mathbf{B} \parallel c^*$. These are compared to the experimental data of Ref. 10 at $T < 2$ K. We thus find good agreement. To probe for field-induced phase transitions of the model, we show in Fig. S1(b) the fidelity susceptibility $\chi_F = [2/(\delta B)^2][1 - \langle \Psi_0(B) | \Psi_0(B + \delta B) \rangle]$ and the second derivative of the ground state energy ($-\partial^2 E_0 / \partial B^2$) for in-plane fields $\mathbf{B} \parallel b$. These reveal

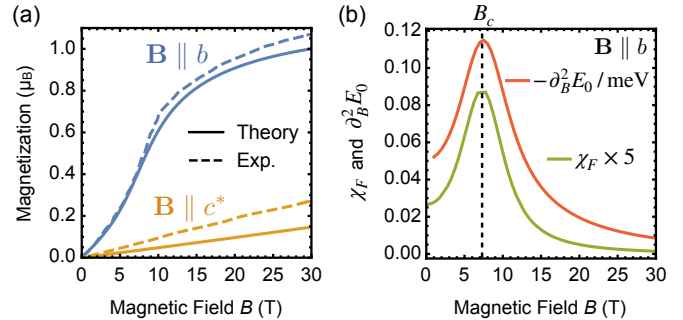


FIG. S1. Field-strength-dependent ED results on the model $\{\mathcal{J}|_{\epsilon=0}\}$ of Table I in the main text. (a) Magnetization for $\mathbf{B} \parallel b$ (in-plane) and $\mathbf{B} \parallel c^*$ (out-of-plane). Dashed curves show experimental data from Ref. 10. (b) Second derivative of the ground-state energy and fidelity susceptibility χ_F .

a single phase transition as a function of field strength at $B_c \approx 7.5$ T, between the low-field zigzag ordered phase and the high-field partially-polarized phase. The critical field for the perpendicular direction within the honeycomb plane ($\mathbf{B} \parallel a$) is found to be similar, while zigzag order is much more stable for fields perpendicular to the plane ($\mathbf{B} \parallel c^*$) with $B_c \approx 82$ T. These results are all consistent with experiment, and the physics are analogous to those described in the context of a minimal magnetic model in Ref. 49.

In Fig. S2(a) we show the field-angle-dependent magnetic torque $\tau \equiv dE/d\theta$ as a function of the out-of-plane angle θ . $\theta = 0$ corresponds to the in-plane direction b and $\theta = 90^\circ$ to the out-of-plane direction c^* . The essential evolution with field-angle and field-strength and the characteristic sawtooth-shape reproduce the experiments [50–52] well. Fig. S2(b) shows the magnetotropic coefficient $k \equiv d\tau/d\theta$, which is also in good qualitative agreement with experiment [51, 53]. The distinct behaviors of τ and k in the present model are consequences of the significant Γ_1 interaction and g-anisotropy ($g_{ab} > g_{c^*}$) [54].

Derivation of Equations (3) and (4) of the main text

We derive Eqs. (3) and (4) of the main text. These were used to estimate the field-dependent magnetostriction $\lambda_{c^*} \equiv L_{c^*}^{-1}(\partial L_{c^*} / \partial B) = \partial \epsilon / \partial B$ and the structural Grüneisen parameter $\Gamma_s \equiv -\frac{(\partial S_m / \partial p_{c^*})}{T(\partial S_m / \partial T)}$. Here, L_{c^*} is the length of the crystal along c^* , S_m the magnetic entropy and p_{c^*} uniaxial pressure along c^* . We start with the general expression of the change in the Gibbs free en-

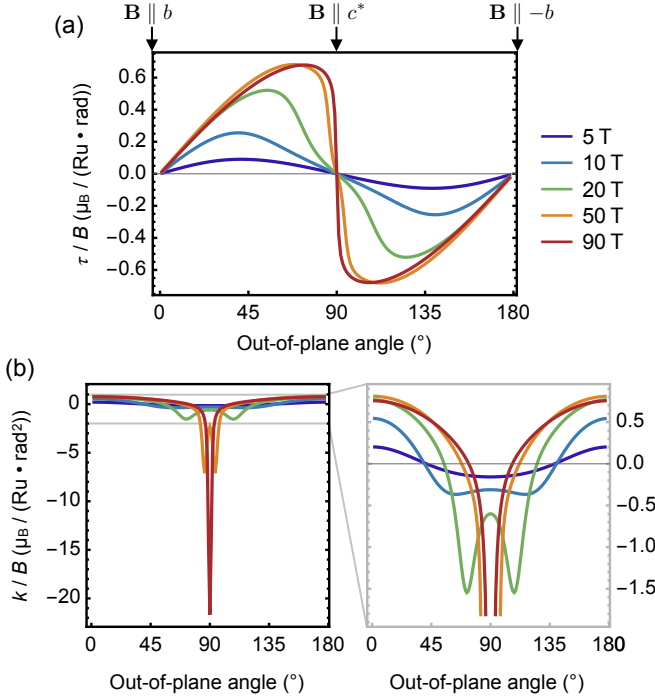


FIG. S2. Field-angle-dependent ED results on the model $\{\mathcal{J}|_{\epsilon=0}\}$ of Table I in the main text. The field-direction rotates from b (in-plane) over c^* (out-of-plane) to $-b$. (a) Magnetic torque normalized by field strength, $\tau/B = (dE/d\theta)/B$. (b) Normalized magnetotropic coefficient $k/B = (d\tau/d\theta)/B$. The lower-right panel shows a narrower plot range for k/B .

ergy under consideration of anisotropic strain and stress contributions

$$d\mathcal{G} = \sum_{ij} \epsilon_{ij} d\sigma_{ij} - S dT - M dB, \quad (\text{S1})$$

with the strain tensor ϵ_{ij} , the stress tensor σ_{ij} and the crystallographic indices $i, j \in \{a, b, c^*\}$. Note that throughout the main text we have used the shorthand notation $\epsilon_{c^*c^*} \equiv \epsilon$ for uniaxial strain onto c^* . Equation (S1) implies a Maxwell relation for the magnetostriction

$$\lambda_{c^*} = \left(\frac{\partial \epsilon_{c^*c^*}}{\partial B} \right)_{T, \{\sigma_{ij}\}} = \left(\frac{\partial M}{\partial \sigma_{c^*c^*}} \right)_{T, B, \{\sigma_{ij}\} \setminus \{\sigma_{c^*c^*}\}}. \quad (\text{S2})$$

Here, the subscript $\{\sigma_{ij}\}$ denotes that all stress-components are held constant, while $\{\sigma_{ij}\} \setminus \{\sigma_{c^*c^*}\}$ holds all stresses except $\sigma_{c^*c^*}$ constant.

The right-hand side of Eq. (S2) can also be expressed through the elasticity tensor c_{ijkl} , which connects the strain and stress tensors through

$$\sigma_{ij} = \sum_{kl} c_{ijkl} \epsilon_{kl}. \quad (\text{S3})$$

Then, we have with Eqs. (S2) and (S3):

$$\left(\frac{\partial M}{\partial \sigma_{c^*c^*}} \right)_X = \left[\sum_{ij} c_{c^*c^*ij} \left(\frac{\partial \epsilon_{ij}}{\partial M} \right)_X \right]^{-1}, \quad (\text{S4})$$

where the variables $X = (T, B, \{\sigma_{ij}\} \setminus \{\sigma_{c^*c^*}\})$ are held constant in the derivatives.

We now employ the assumption that the elasticity contribution along the direction of the investigated length change ΔL_{c^*} is dominant, i.e., $c_{c^*c^*c^*c^*} \gg c_{c^*c^*ij}$ for $i, j \neq c^*$. Then we can approximate the magnetostriction as

$$\lambda_{c^*} \approx \frac{\kappa_{c^*c^*}}{V} \left(\frac{\partial M}{\partial \epsilon_{c^*c^*}} \right)_X, \quad (\text{S5})$$

where we expressed $c_{c^*c^*c^*c^*}$ through the linear compressibility under uniaxial pressure $\kappa_{c^*c^*} = -\frac{\partial \epsilon_{c^*c^*}}{\partial p_{c^*}} = -V \frac{\partial \epsilon_{c^*c^*}}{\partial \sigma_{c^*c^*}} = -V c_{c^*c^*c^*c^*}^{-1}$. Note that the derivative in Eq. (S5) does importantly *not* hold the other lattice constants a, b or the atom positions constant. Instead these degrees of freedom need to be evolved to their new equilibrium positions when $\epsilon_{c^*c^*}$ is varied, i.e., the structure needs to be relaxed under constrained variations of $\epsilon_{c^*c^*}$, as we have done.

In Eq. (S5), a change in $\epsilon_{c^*c^*}$ affects the magnetization M through the variation of the magnetic interactions \mathbb{J}_{ij} and of the g -tensor \mathbb{G} of the pseudospins. This can be expressed formally by applying the chain rule on Eq. (S5), which leads to

$$\lambda_{c^*} \approx \frac{\kappa_{c^*c^*}}{V} \sum_{\mathcal{J} \in \mathbb{J}_{ij}, \mathbb{G}} \left[\left(\frac{\partial M}{\partial \mathcal{J}} \right) \left(\frac{\partial \mathcal{J}}{\partial \epsilon_{c^*c^*}} \right) \right]_X. \quad (\text{S6})$$

Since $\kappa_{c^*c^*}$ is, up to our knowledge, not known for α -RuCl₃, we can not predict the absolute change in $\epsilon_{c^*c^*}$ under magnetic field, but instead compute $\lambda_{c^*}/\kappa_{c^*c^*}$. We thus have to evaluate the derivatives in Eq. (S6) at $\epsilon_{c^*c^*} = 0$. While this is an approximation at finite fields, we note that the total integrated field-induced change of $\epsilon_{c^*c^*}$ is below 0.1% at $B = 15$ T [46], despite α -RuCl₃ having a comparatively large magnetostriction effect. The influence of such small field-induced changes in $\epsilon_{c^*c^*}$ onto the field-dependence on the contributions in Eq. (S6) is therefore negligible, cf. Figs. S6 and S7. Instead, the main dependence on magnetic field in Eq. (S6) is expected to be carried by the field-dependent derivatives of the magnetization, $\partial M/\partial \mathcal{J}$. With the definition $\tilde{\mathcal{J}} \equiv (\partial \mathcal{J}/\partial \epsilon_{c^*c^*})|_{\epsilon_{c^*c^*}=0}$ we thus arrive at

$$\lambda_{c^*} \approx \frac{\kappa_{c^*c^*}}{V} \sum_{\mathcal{J} \in \mathbb{J}_{ij}, \mathbb{G}} \tilde{\mathcal{J}} \left(\frac{\partial M}{\partial \mathcal{J}} \right)_{X, \epsilon_{c^*c^*}=0}, \quad (\text{S7})$$

which coincides with Eq. (3) of the main text.

For the structural Grüneisen parameter $\Gamma_s \equiv -\frac{\partial S_m/\partial \sigma_{c^*c^*}}{VT(\partial S_m/\partial T)}$, an analogous approach can be made,

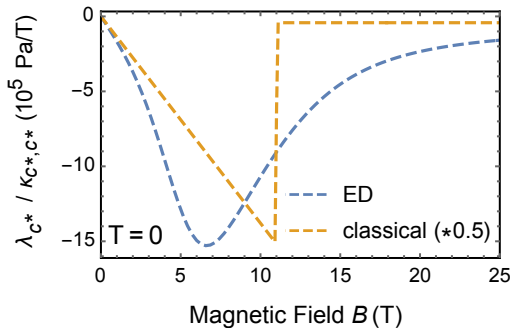


FIG. S3. Comparison of ED and classical results for the field-dependent magnetostriction of the minimal magnetic model $\{\mathcal{J}|_{\epsilon=0}\}$ of Ref. 55 in conjunction with our magnetoelastic couplings $\tilde{\mathcal{J}}$ from main-text Table I. Classical result is divided by a factor of 2.

where in Eq. (S4) M is replaced with S_m . Analogously one arrives at

$$\Gamma_s \approx \frac{\kappa_{c^*c^*}}{T} \sum_{\mathcal{J} \in \mathbb{J}_{ij}, \mathbb{G}} \tilde{\mathcal{J}} \left(\frac{\partial S_m}{\partial \mathcal{J}} \right)_{\epsilon_{c^*c^*}=0} \left(\frac{\partial S_m}{\partial T} \right)_{\epsilon_{c^*c^*}=0}^{-1}, \quad (\text{S8})$$

which coincides with Eq. (4) of the main text.

Classical results for magnetostriction

The results presented in Fig. 4 of the main text are effected by finite-size effects of the 24-site ED calculations. Here we compare to a classical calculation of the $T = 0$ magnetostriction, that is free of finite-size effects. For this, the magnetization susceptibilities $(\partial M / \partial \mathcal{J})$ in Eq. (S7) are evaluated by classical energy minimization of the minimal magnetic model $\{\mathcal{J}|_{\epsilon=0}\}$ of Ref. 55 while the magnetoelastic couplings $\tilde{\mathcal{J}}$ are taken from Table I (main text). An analogous classical calculation is not possible on the full *ab-initio*-derived model of Table I (main text) as that model does not have a zigzag ground state on the classical level, but the insights likely apply also to that model.

Results are shown in Fig. S3. Note that the classical result is divided by a factor of 2 for better comparability. Aside from the increased overall magnitude compared to the ED result, the drop of the magnitude $|\lambda_{c^*}|$ when leaving the zigzag phase is much more pronounced here, which is more consistent with experiment. A smearing-out of phase transitions is expected as a typical finite-size effect in ED. However, the classical result lacks the quantum fluctuations that are present in ED, such that the critical field strength is overestimated ($B_{c,\text{classical}} = 11$ T, $B_{c,\text{ED}} = 6$ T).

Both in the classical and in the ED results, we note that the dominating contribution to λ_{c^*} comes from the summand in Eq. (S7) that describes magnetoelastic cou-

pling from $\tilde{\Gamma}'_1$. An increase in Γ'_1 lowers the in-plane critical field strength [56], such that —within the zigzag phase $B < B_c$ — spins are more strongly canted towards the direction of the magnetic field for a given field strength B , i.e., have higher magnetization. Therefore $(\partial M / \partial \Gamma'_1) > 0$, which together with $\tilde{\Gamma}'_1 < 0$ [Table I (main text)] explains an overall *negative* sign of the magnetostriction.

Details on structural Grüneisen parameter

The structural Grüneisen parameter $\Gamma_s \equiv -\frac{(\partial S_m / \partial p_{c^*})}{T(\partial S_m / \partial T)}$ can not be obtained from a pure ground state calculation (where the entropy would vanish). As we are interested in low-but-finite temperature calculations, we employ a method where we restrict the canonical sums to the lowest d_c eigenstates,

$$Z \approx \sum_{n=0}^{d_c-1} e^{-E_n / (k_B T)},$$

$$\langle O \rangle \approx \frac{1}{Z} \sum_{n=0}^{d_c-1} e^{-E_n / (k_B T)} \langle n | O | n \rangle, \quad (\text{S9})$$

which has proven reliable for calculations of the magnetic Grüneisen parameter Γ_B [57]. We use Eq. (S9) to evaluate the structural Grüneisen parameter at $T = 4$ K via Eq. (S8) and ED with up to $d_c = 16$. The dependence on d_c of our results is shown in Fig. S4(b), which corresponds for $d_c = 16$ to the solid line in Fig. 4(c) of the main text. As these results are very robust already for $d_c > 3$, we deem the results very reliable. In Fig. S4(d) we show the error analysis for the case where the minimal magnetic model of Ref. 55 is used for the $\mathcal{J}|_{\epsilon=0}$ couplings. Here, results appear not fully converged at $T = 4$ K, but we assume trends to be correct. This can also be seen at the exact $T = 0$ result shown in Fig. S4(c) of the same model. Here an exact evaluation is possible as the $T \rightarrow 0$ limit of a Grüneisen parameter is only determined by the behavior of the gap between the ground state and lowest excited state [57].

Inspecting the zero-temperature limit of Γ_s in our full *ab-initio* model from the main-text Table I, shown in Fig. S4(a), a discontinuity is apparent at $B = 22.5$ T. This is the result of a level crossing in the first two excited states at this field strength, which produces such an anomaly in all Grüneisen parameters of the form $\Gamma_\lambda \equiv -\frac{\partial S / \partial \lambda}{T(\partial S / \partial T)}$ [57]. At small finite temperatures [blue curve in Fig. S4(a)], the discontinuity is smeared out to a shoulderlike feature, and is mostly invisible for intermediate and high temperatures, as in Fig. S4(b) for $T = 4$ K. An analogous shoulder-anomaly has been observed experimentally in the *magnetic* Grüneisen parameter Γ_B at $B \sim 10$ T, that resembles the anomaly in Γ_B in our model [57]. While the location of the shoulder-anomalies in this

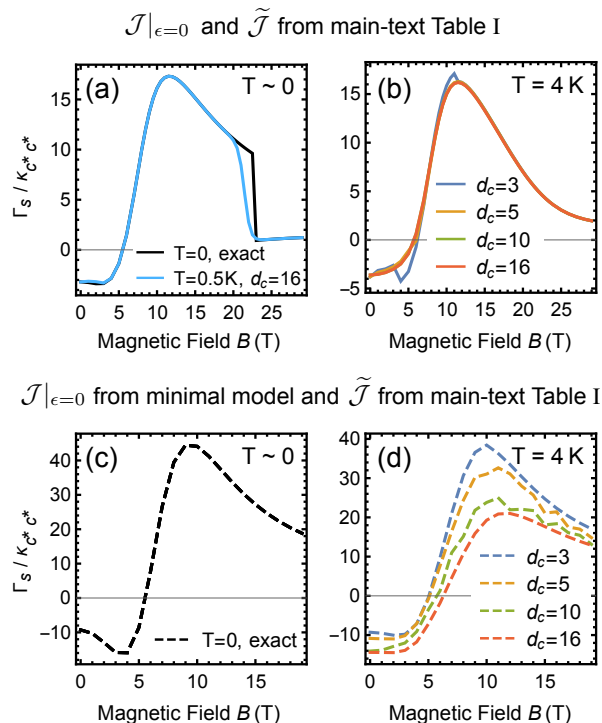


FIG. S4. Detailed results on temperature-dependence and estimation of the cutoff errors for the structural Grüneisen parameter Γ_s . Top panels (a,b) show results for $\mathcal{J}|_{\epsilon=0}$ and $\tilde{\mathcal{J}}$ from main-text Table I, bottom panels (c,d) show results for $J|_{\epsilon=0}$ from the minimal magnetic model of Ref. 55 and $\tilde{\mathcal{J}}$ from main-text Table I. (a,c) Zero- and low-temperature results. (b,d) Results at $T = 4$ K for different employed cutoffs d_c (see Eq. (S9)).

model and experiment appear far apart in field strength, we note that —up to our knowledge— no other realistic model proposed so far for α - RuCl_3 (including the minimal model [55] we discussed) features any such shoulder-anomaly in Grüneisen parameters. In the present model, a level crossing between the lowest excited states, that produces the shoulder-anomaly, happens between states at $\mathbf{k} = Y$ and $\mathbf{k} = 0$. We interpret this to be a result of the strongly competing ferromagnetic phase (with ordering wave vector $\mathbf{q} = 0$) in the present model. As the precise field strength at which the anomaly occurs is highly sensitive to the coupling strengths, future refinements of the model may take this into account.

We note that the present full *ab-initio* model predicts the low-temperature shoulder anomaly to be significantly stronger in the structural Grüneisen parameter Γ_s [Fig. S4(a)] than in the magnetic Grüneisen parameter Γ_B [57]. Since the field strength at which the anomaly takes place is overestimated in this model, the actual drop in Γ_s might occur already at $B \approx 10$ T [57]. Accordingly, a small dip in Γ_s is suggested by experimental data at $T = 3.5$ K [46].

Further Details of First-principles Calculations

Structural relaxation.— The constrained relaxations were performed using *ab-initio* DFT as implemented in the QUANTUM ESPRESSO (QE) package [58] in zigzag antiferromagnetic configurations of ruthenium. A plane-wave basis set was used to expand the electronic wave functions and the exchange-correlation functional was approximated by the generalized gradient approximation (GGA+ U) of Perdew, Burke, and Ernzerhof [59] with $U = 1.5$ eV. The cutoff for the plane-wave basis set and the cutoff for the corresponding charge densities were set at 60 and 600 Ry, respectively. We considered Van-der-Waals corrections within Grimme’s DFT-D2 method [60]. A Monkhorst-Pack [61] grid of size $8 \times 6 \times 8$ was used to generate the k-mesh (zone centered) for the corresponding Brillouin-zone sampling.

In order to check the effects of spin-orbit coupling (SOC) on the relaxation, we used VASP code [62] using the projector-augmented plane-wave basis [63]. For this, the unstrained structural optimization at ambient pressure was recalculated with VASP in the GGA+ U approximation and the results from the two methods were found to agree well. Then the former code was used to find the effect of SOC (within GGA+ U +SOC) on the lattice geometry. We find that SOC mainly brings the structure further to approximate C_3 symmetry of the honeycomb planes. This effect is in line with other studies of honeycomb ruthenates, iridates and rhodates [64–66] and consistent with the approximately C_3 -symmetric magnetic response observed in α - RuCl_3 [10, 67–69]. These observations also vindicate our work with a C_3 -simplified version of the obtained model throughout the discussions in the main text. In Table SI we give the full model before C_3 symmetrization, where coupling strengths on Z bonds can differ from those on X/Y bonds. The rows $\mathcal{J}_{3\text{orb}}$ and $\tilde{\mathcal{J}}_{3\text{orb}}$ in this table show results not including effects of all 5 orbitals, that are compared below.

Exchange interaction calculations.— With the structural response toward uniaxial strain ϵ established, each structure can be associated with a magnetic Hamiltonian determined by \mathbb{J}_{ij} and \mathbb{G} (see Eq. (1) of the main text). To extract the corresponding coupling parameters $\mathcal{J} \in \mathbb{J}_{ij}$, we first construct the multi-orbital Hubbard Hamiltonian for the ruthenium sites.

For the two-particle interaction terms, we used spherically symmetric expressions [70], parametrized by Slater integrals, and fixing them to values based on recent cRPA results for α - RuCl_3 [71]. The local two-particle exchange parameters were obtained by subtraction of the non-local contributions given in Ref. 71. Averaging over the orbital-dependent expression and taking an effective two-particle on-site interaction then lead to the parameters employed in this work, $U_{t_{2g}} = F_0 + (4/49)(F_2 + F_4) = 1.68$ eV and $J_{t_{2g}} = (3/49)F_2 + (20/441)F_4 = 0.29$ eV.

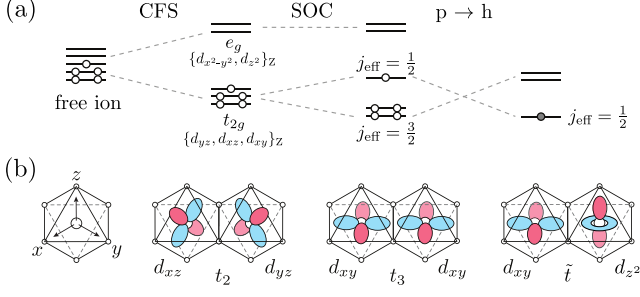


FIG. S5. (a) Effects of crystal field splitting (CFS), spin-orbit coupling (SOC) and a particle-hole ($p \rightarrow h$) transformation in a d^5 configuration. (b) Dominant hopping processes t_2 , t_3 and \tilde{t} on the Z-bond for the experimental structure of α -RuCl₃, explicitly given in Eq. (S10).

The material-specific properties are encoded in the first-principles ruthenium hopping parameters. As illustrated in Fig. S5(a), the crystal field splitting (CFS) due to the octahedral chlorine environment causes a splitting between energetically low t_{2g} orbitals and the higher in energy e_g orbitals. Due to the energy gap the low-energy properties of the system can be described in terms of a low-spin configuration, where the electrons populate the t_{2g} orbitals. Spin-orbit coupling (SOC) was included in the atomic approximation with a SOC parameter $\lambda = 0.15$ eV [72]. Considering such strong spin-orbit coupling, the t_{2g} orbitals form together with the spin 1/2 degree of freedom $j_{\text{eff}} = 1/2$ and $j_{\text{eff}} = 3/2$ states [see Fig. S5(a)]. Since the $j_{\text{eff}} = 3/2$ states are fully occupied, exact diagonalization of the two-site five-orbital Hubbard Hamiltonian then allows to project the determined low-energy states onto a bilinear pseudospin 1/2 Hamiltonian. The resulting bond-resolved first-principles coupling parameters up to third-nearest neighbors at $\epsilon = 0$ are shown in Table SI. C_3 -symmetrization of these values lead to the parameters given in the main text.

Effects of e_g orbitals

Although the nearest-neighbor Kitaev interaction was introduced within the three-orbital t_{2g} framework of the Khaliullin-Jackeli mechanism [2, 3, 73], the role of e_g orbitals for Kitaev materials was previously considered in some approximations [13, 74, 75]. In this work, we extended the approach by some of the authors [76], where the Hubbard Hamiltonian was constructed with only t_{2g} ruthenium orbitals. Interestingly, inclusion of the e_g orbitals leads to an increase of the magnitudes of the g tensor components as well as the bilinear magnetic interactions, given in Table SI, including the ferromagnetic nearest-neighbor Kitaev interaction K_1 . Meanwhile, the magnetoelastic couplings are in most cases overestimated if e_g effects are neglected.

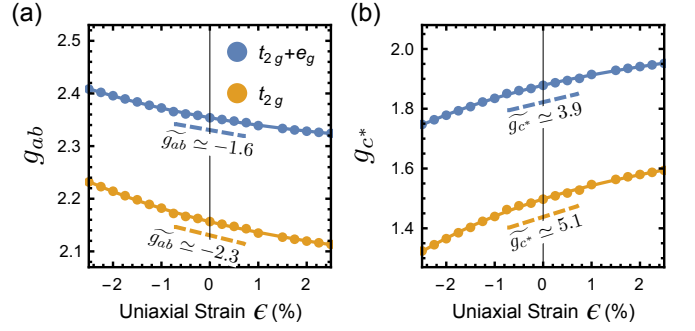


FIG. S6. g -values at different uniaxial strains ϵ , either taking into account only the t_{2g} orbitals [CAS(5,3)] or all five d -orbitals [$t_{2g} + e_g$; CAS(5,5)]. Solid lines show third-order polynomial fits. Values next to dashed lines indicate $\tilde{\mathcal{J}} \equiv (\partial J / \partial \epsilon)|_{\epsilon=0}$.

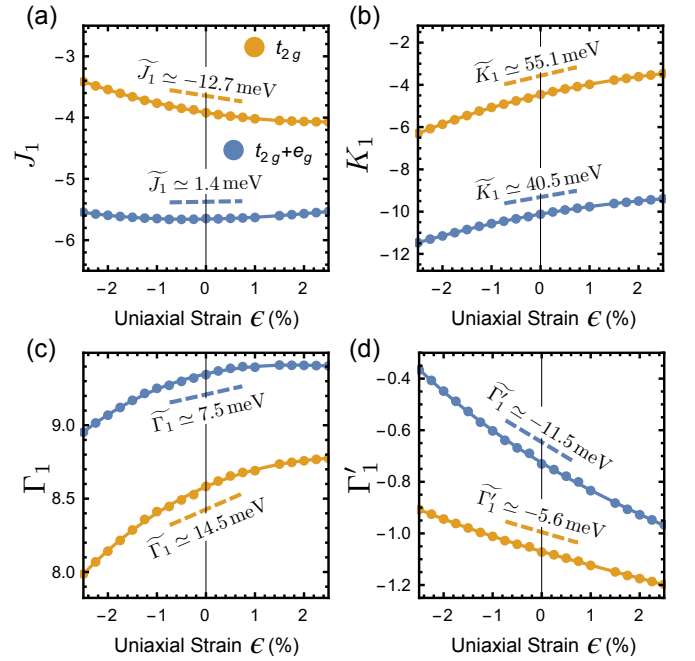


FIG. S7. Nearest-neighbor magnetic interactions at different uniaxial strains ϵ , either taking into account only the t_{2g} orbitals or all five d -orbitals ($t_{2g} + e_g$). Solid lines show third-order polynomial fits. Values next to dashed lines indicate $\tilde{\mathcal{J}} \equiv (\partial J / \partial \epsilon)|_{\epsilon=0}$.

If only t_{2g} orbitals were considered, the relevant Hilbert space could be reduced by a particle-hole transformation, which results in a projection of the one-hole low-energy solution onto pseudospin 1/2 operators [see Fig. S5(a)]. Additional consideration of e_g orbitals within this procedure takes higher-order hopping processes into account that lead to corrections of the final effective pseudospin Hamiltonian. The present analysis is limited to two-site clusters, which likely leads to underestimation of second and third neighbor couplings, which were found to be of non-negligible magnitude [76, 77]. However, this

	g_a	g_b	g_{c^*}	J_1	K_1	Γ_1	Γ'_1	J_2	K_2	Γ_2	Γ'_2	D_2^α	D_2^β	D_2^γ	J_3	K_3	Γ_3	Γ'_3
$\widetilde{\mathcal{J}}_{5\text{orb}}^Z$	2.27	2.44	1.88	-5.	-12.4	6.9	-1.2	0.	-0.1	0.	-0.	0.	0.	0.2	0.3	0.2	0.1	-0.1
$\widetilde{\mathcal{J}}_{5\text{orb}}^X$				-6.	-9.	10.6	-0.5	0.	-0.2	0.1	0.1	0.	0.1	0.	0.2	0.3	0.2	-0.1
$\widetilde{\mathcal{J}}_{3\text{orb}}^Z$	2.07	2.25	1.50	-2.4	-7.7	5.5	-1.4	-0.3	-0.6	0.1	-0.2	-0.	-0.	0.	0.3	0.3	-0.1	-0.1
$\widetilde{\mathcal{J}}_{3\text{orb}}^X$				-4.7	-2.9	10.1	-0.9	-0.8	0.5	-0.1	0.1	-0.1	0.1	-0.1	0.1	0.3	-0.2	-0.2
$\widetilde{\mathcal{J}}_{5\text{orb}}^Z$	-1.38	-1.84	3.85	-15.8	35.	3.4	-9.1	-1.4	1.9	-0.8	-0.4	-1.	-1.	-3.9	3.8	1.	-0.4	-0.5
$\widetilde{\mathcal{J}}_{5\text{orb}}^X$				9.9	43.3	9.5	-12.7	-0.6	1.4	-0.3	0.1	-1.3	-0.8	-2.8	0.6	0.3	-0.7	-0.5
$\widetilde{\mathcal{J}}_{3\text{orb}}^Z$	-2.08	-2.43	5.07	-9.4	43.3	8.	-1.8	0.4	2.4	-1.4	-0.8	-1.	-1.	-2.8	3.5	1.6	-1.3	-0.8
$\widetilde{\mathcal{J}}_{3\text{orb}}^X$				-14.3	61.	17.8	-7.5	-0.4	0.6	-0.6	-0.2	-1.4	-0.4	-1.9	0.1	0.4	-1.	-0.7

TABLE SI. g -tensor components and magnetic interactions $\mathcal{J}^Z|_{\epsilon=0}$ ($\mathcal{J}^X|_{\epsilon=0}$) on Z-bonds (X-bonds) in meV for the zero-strain relaxed $C2/m$ structure before C_3 symmetrization and with hopping parameters considering all five Ru 4d orbitals ($\mathcal{J}_{5\text{orb}}$) compared to only Ru t_{2g} orbitals ($\mathcal{J}_{3\text{orb}}$). Y bonds are related to X bonds by mirror symmetry.

restriction is necessary to limit computational expense.

In order to highlight the effects of the e_g orbitals on the g -tensor, we compare the results obtained from ORCA [78] at the CASSCF/TPSSH/def2-TZVP level on $[\text{RuCl}_6]^{3-}$ clusters, using active space definitions of (5,3) and (5,5). The former explicitly excludes any configurations with partial occupancy of the e_g orbitals, while the latter includes those configurations. In both cases, we considered equal weight on all doublet states in the orbital optimization. The e_g effects for the C_3 -symmetrized g tensor components as a function of uniaxial strain ϵ are illustrated in Fig. S6. At $\epsilon = 0$, the full approach considering $(t_{2g} + e_g)$ orbitals reveals an increased magnitude for both, g_{ab} and g_{c^*} . This increase is not homogeneous, leading to a reduction of the anisotropy g_{ab}/g_{c^*} . Considering the non-symmetrized values in Table SI, it also becomes evident that the anisotropy within the honeycomb plane, i.e., $g_a < g_b$, is reduced by e_g effects. The magnetoelastic couplings \widetilde{g}_{ab} and \widetilde{g}_{c^*} are reduced upon consideration of these effects, so that an overestimation of the coupling to the lattice can be prevented by consideration of such higher-order processes.

In Fig. S7 we compare strain-dependent nearest-neighbor magnetic interactions considering t_{2g} and $(t_{2g} + e_g)$ orbitals. In this case, e_g effects can be related to the first-principles hopping parameters between them and the low-energy t_{2g} orbitals. For the $\epsilon = 0$ structure we computed the following parameters on the Z-bond (the bond parallel to the b direction, see Fig. 1 of the main text):

$$t_Z = \begin{pmatrix} & d_{yz} & d_{xz} & d_{xy} & d_{x^2-y^2} & d_{z^2} \\ d_{yz} & +0.04 & +\mathbf{0.15} & -0.01 & 0 & 0 \\ d_{xz} & +\mathbf{0.15} & +0.04 & -0.01 & 0 & 0 \\ d_{xy} & -0.01 & -0.01 & -\mathbf{0.08} & 0 & +\mathbf{0.28} \\ d_{x^2-y^2} & 0 & 0 & 0 & -0.01 & 0 \\ d_{z^2} & 0 & 0 & +\mathbf{0.28} & 0 & 0 \end{pmatrix} \quad (\text{S10})$$

The highlighted dominant hopping mechanisms are illustrated in Fig. S5(b). While t_2 and t_3 are strong hoppings

within the t_{2g} orbitals, we find the strongest hopping to be \tilde{t} , which connects the t_{2g} orbital d_{xy} with the e_g orbital d_{z^2} .

Consideration of this additional large exchange mechanism leads to a reshuffling of relative coupling strengths with an overall tendency to an increase in magnitude (see also Table SI). For K_1 , Γ_1 , and J_1 , the absolute value increases including e_g orbitals. The only reduced nearest-neighbor interaction is Γ'_1 .

The magnetoelastic couplings $\widetilde{\mathcal{J}}$ are given in Table SI and are illustrated by the slope of the dashed lines in Fig. S7. For most interaction parameters they follow the same trend when including e_g effects, but become reduced in magnitude. Exceptions are $\widetilde{\Gamma}'_1$ and $\widetilde{\mathcal{J}}_1$: For $\widetilde{\Gamma}'_1$ the inclusion of e_g effects leads to a strongly *enhanced* magnetoelastic coupling compared to the 3-orbital result. For $\widetilde{\mathcal{J}}_1$, the five-orbital result shows differing signs on Z and X/Y bonds. This leads to a (possibly artificially) small value of the C_3 -symmetrized $\widetilde{\mathcal{J}}_1 = (2\widetilde{\mathcal{J}}_1^X + \widetilde{\mathcal{J}}_1^Z)/3$. However, as the experimentally accessible magnetostriction and structural Grüneisen parameter are dominated by the $\widetilde{\Gamma}'_1$ response, this issue has little consequence for the quantities discussed in this work and we therefore decided to keep the discussion in the C_3 -symmetrized limit.

We therefore conclude that the interplay of higher order hopping processes together with the structure of Hund's coupling in d block elements lead to a delicate coupling between magnetism and structure that—to the best of our knowledge—has not been captured with analytical methods such as perturbation theory so far.

Inter-plane couplings

In $\alpha\text{-RuCl}_3$, most phenomena have generally been well captured qualitatively in terms of quasi-two-dimensional descriptions, that neglect inter-plane magnetic couplings between the van-der-Waals layers [3, 45, 79]. As uniaxial strain along c^* however affects the distance between the honeycomb planes stronger than in-

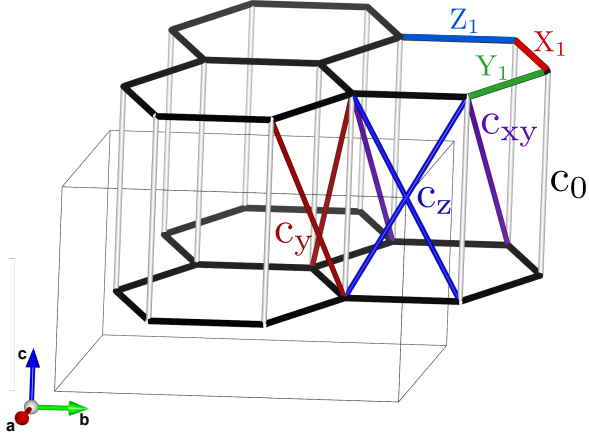


FIG. S8. Four shortest inter-layer bonds in the relaxed $C2/m$ α - RuCl_3 structure at ambient pressure: c_0 connects two ruthenium sites by the crystallographic c axis, c_y is the bond of two sites that are connected by the inter-layer bond c_0 and the intra-layer bond Y_1 , c_z connects sites along c_0 - Z_1 , and c_{xy} connects sites along c_0 - X_1 - Y_1 .

plane distances (see Fig. 2 of the main text), one might suspect *magnetoelastic* couplings related to inter-plane couplings to become significant.

We have therefore calculated the magnetoelastic couplings of the four shortest inter-layer bonds, illustrated in Fig. S8, with the same procedures as described above for the in-plane couplings. For the shortest-distance inter-plane bond, which connects two ruthenium sites by the crystallographic c axis, labeled “ c_0 ”, we extract a magnetic pseudospin interaction $H_{ij} = \mathbf{S}_i \cdot \mathbb{J}_{ij} \cdot \mathbf{S}_j$ with

$$\mathbb{J}_{c_0} = \begin{pmatrix} & x & y & z \\ x & 0.06 & 0.02 & 0.05 \\ y & 0.07 & 0.06 & 0.05 \\ z & 0.07 & 0.07 & -0.06 \end{pmatrix} \text{ meV}, \quad (\text{S11})$$

which is much weaker than the nearest-neighbor in-plane magnetic exchange ($K_1 = -10.1$ meV). For the corresponding magnetoelastic couplings on the same inter-plane bond we extract

$$\widetilde{\mathbb{J}}_{c_0} = \begin{pmatrix} & x & y & z \\ x & -0.67 & 0.47 & -0.37 \\ y & -0.63 & -0.67 & -0.37 \\ z & -0.86 & -0.86 & 0.4 \end{pmatrix} \text{ meV} \quad (\text{S12})$$

which should be compared to the in-plane $\widetilde{K}_1 = 40.5$ meV and $\widetilde{\Gamma}'_1 = -11.5$ meV.

We labelled the next-shortest inter-layer bond “ c_y ”, which is the bond of two sites that are connected by

the inter-layer bond c_0 and the intra-layer bond Y_1 (see Fig. S8). We find the couplings to be of similar order of magnitude:

$$\mathbb{J}_{c_y} = \begin{pmatrix} & x & y & z \\ x & -0.09 & 0.07 & 0.02 \\ y & 0.07 & 0.11 & 0.01 \\ z & 0.02 & 0.01 & 0.09 \end{pmatrix} \text{ meV}. \quad (\text{S13})$$

Interestingly, the corresponding magnetoelastic couplings are slightly increased compared to the values for bond c_0 :

$$\widetilde{\mathbb{J}}_{c_y} = \begin{pmatrix} & x & y & z \\ x & 0.04 & -0.17 & -0.28 \\ y & -0.17 & -1.24 & 0.27 \\ z & -0.28 & 0.27 & -0.86 \end{pmatrix} \text{ meV} \quad (\text{S14})$$

The same is true for the c_z bond that connects sites along the path c_0 - Z_1 :

$$\mathbb{J}_{c_z} = \begin{pmatrix} & x & y & z \\ x & 0.08 & -0.01 & -0.03 \\ y & -0.01 & 0.2 & -0.03 \\ z & -0.03 & -0.03 & 0.03 \end{pmatrix} \text{ meV}, \quad (\text{S15})$$

with

$$\widetilde{\mathbb{J}}_{c_z} = \begin{pmatrix} & x & y & z \\ x & -1.59 & 0. & 0.06 \\ y & 0. & -3.19 & 0.06 \\ z & 0.06 & 0.06 & -0.89 \end{pmatrix} \text{ meV}. \quad (\text{S16})$$

Finally, two sites connected by the path c_0 - X_1 - Y_1 contain slightly smaller couplings and magnetoelastic couplings:

$$\mathbb{J}_{c_{xy}} = \begin{pmatrix} & x & y & z \\ x & 0.05 & -0.06 & 0.08 \\ y & 0.1 & 0.05 & 0.08 \\ z & -0.13 & -0.13 & 0.17 \end{pmatrix} \text{ meV}, \quad (\text{S17})$$

with

$$\widetilde{\mathbb{J}}_{c_{xy}} = \begin{pmatrix} & x & y & z \\ x & 0.29 & -0.48 & -0.63 \\ y & -0.63 & 0.29 & -0.63 \\ z & 0.74 & 0.74 & -0.46 \end{pmatrix} \text{ meV} \quad (\text{S18})$$

Inter-plane couplings have therefore been neglected in the discussion of magnetostriction and structural Grüneisen parameter.